Pit initiation in quenching and partitioning processed martensitic stainless steels

Li, Gaojie; Li, Ziyu; Rahimi, Ehsan; Muratori, Marta; Smith, Ali; Santofimia, Maria Jesus; Gonzalez-Garcia, Yaiza

DOI
10.1016/j.electacta.2024.144646

Publication date
2024

Document Version
Final published version

Published in
Electrochimica Acta

Citation (APA)
Li, G., Li, Z., Rahimi, E., Muratori, M., Smith, A., Santofimia, M. J., & Gonzalez-Garcia, Y. (2024). Pit initiation in quenching and partitioning processed martensitic stainless steels. *Electrochimica Acta*, *498*, Article 144646. https://doi.org/10.1016/j.electacta.2024.144646

Electrochimica Acta 498 (2024) 144646

Contents lists available at ScienceDirect

Electrochimica Acta

journal homepage: www.journals.elsevier.com/electrochimica-acta

Pit initiation in quenching and partitioning processed martensitic stainless steels

Gaojie Li [a,*], Ziyu Li [a], Ehsan Rahimi [a], Marta Muratori [b], Ali Smith [c], Maria J. Santofimia Navarro [a], Yaiza Gonzalez-Garcia [a]

[a] *Department of Materials Science and Engineering, Delft University of Technology, Mekelweg 2, 2628 CD Delft, the Netherlands*
[b] *Acerinox Europa S.A.U., Acerinox Europa Av, 11379 Los Barrios, Spain*
[c] *RINA Consulting - Centro Sviluppo Materiali SpA, Castel Romano 100, 00128 Rome, Italy*

ARTICLE INFO

Keywords:
Q&P stainless steels
Inclusions
AFM/SKPFM
SECM
Pitting corrosion
XPS

ABSTRACT

The present article investigates the influence of chemical composition and phase fractions on the corrosion behaviour of industrially produced quenching and partitioning (Q&P) martensitic stainless steels. Localised corrosion was analysed by scanning Kelvin probe force microscopy (SKPFM) and scanning electrochemical microscopy (SECM) in 3.5 wt.% NaCl solution. SKPFM revealed a Volta-potential difference of around 40 mV between inclusions and the matrix, which is larger than the Volta potential variations within the matrix. This difference in surface potential is a driving force for selective dissolution (corrosion initiation) at inclusions and inclusion/matrix interfaces. SECM detected early pitting initiation, particularly in alloys containing MnS and TiN inclusions. Results suggest that pitting initiation and propagation occur at those specific regions. This study emphasised that irrespective of chemical composition and phase fraction, localised corrosion initiation in Q&P-processed martensitic stainless steels is predominantly governed by the presence of inclusions.

1. Introduction

The wish to reduce energy consumption and the demand for lighter vehicles producing lower CO_2 emissions has led to considerable progress in the development of advanced high-strength steels (AHSS) for automotive applications [1–3]. The quenching and partitioning (Q&P) treatment has pushed further the boundaries in terms of realisable strength and ductility combinations [4–6]. The Q&P treatment involves a quenching step in which a controlled fraction of martensite is formed, followed by an isothermal treatment aiming at the partitioning of carbon from the martensite into the untransformed austenite [7]. The resulting microstructure is formed by carbon-depleted martensite and carbon-enriched retained austenite. Extensive reports on the Q&P treatment applied to carbon steels [2,8–10] have shown a superior combination of strength and toughness due to the combination of martensite and retained austenite.

Furthermore, the Q&P treatment can be successfully applied to stainless steels, leading to high-strength martensitic stainless steels [11–16]. Investigations on Q&P-processed martensitic stainless steels have mainly focused on the relationship between microstructure and mechanical properties [12,13,16,17] and have evidenced the precipitation of carbides in the microstructures [11–16]. The presence of carbides brings concerns regarding the precipitation of Cr-carbides and subsequent Cr depletion, which can affect the corrosion resistance of these steels.

Research on the corrosion performance of Q&P steels reports that both Q&P carbon steels [18,19] and stainless steels [14,16,20] exhibit better corrosion resistance than traditional quenching and tempering (Q&T) steels. In Q&T steels, retained austenite is absent or present in very low fractions (typically less than 0.01). Therefore, carbon is dissolved in the martensite [18,19]. In Q&P steels, the C-depleted martensite is electrochemically more active than the C-rich retained austenite. The total cathodic area (C-rich retained austenite) in the Q&P steels is smaller than in the Q&T steels (C-rich martensite). Thus, the corrosion rate for Q&P steels is lower than for Q&T steels [19]. Moreover, the long tempering treatments applied to Q&T-processed steels (of the order of hours) allow the precipitation of Cr-carbides, leading to Cr-depletion at the carbide-matrix interface region, which is susceptible to the initiation of pitting corrosion. In the case of Q&P steels, the isothermal treatments applied are shorter (typically minutes), reducing,

---

* Corresponding author at: Delft University of Technology, Department of Materials Science and Engineering Mekelweg 2, 2628 CD Delft, the Netherlands.
E-mail address: g.li-6@tudelft.nl (G. Li).

https://doi.org/10.1016/j.electacta.2024.144646
Received 28 March 2024; Received in revised form 25 June 2024; Accepted 29 June 2024

but not eliminating, the chances of Cr-carbide precipitation. Consequently, the Q&P-processed steels might present better pitting corrosion resistance than the conventional Q&T steels [14,16,20].

In industrial production, impurity elements induce inclusions that cannot be completely avoided. Manganese sulphides (MnS), in particular, act as an active site for pitting initiation in a chloride environment [21–31]. It is generally agreed that the existence of MnS inclusions on steel surfaces leads to discontinuities in passive films, and the local dissolution at the MnS sites acts as an initiation of pitting corrosion, which makes the sample surface more easily attacked by chloride ions [25–27].

Incorporating microalloying elements, such as Ti and Nb, in steels is a common strategy [32–37] to improve impact toughness and strength by grain size refinement [33] and precipitation strengthening. This is due to the formation of nano-sized TiN and NbC particles. The combined effect of nano-sized precipitates and the transformation-induced plasticity (TRIP) of retained austenite leads to an exceptional balance between strength and ductility [36]. However, several works have shown the detrimental effect of TiN precipitates in corrosion. These works have investigated localised corrosion initiation at TiN inclusions in Ni-based alloys [38,39], austenitic stainless steel [40], and interstitial-free (IF) steel [41]. Overall, these studies have consistently demonstrated a decrease in corrosion resistance and an increased susceptibility to localised corrosion attacks when TiN inclusions are present. Similar to MnS inclusions, TiN inclusion also serves as a preferential site for initiating corrosion [41,42].

Although corrosion mechanisms involving MnS and TiN inclusions have been investigated in the literature, the specific role of MnS and TiN inclusions in the corrosion resistance of Q&P steels is still not understood. Q&P steels are multiphase steels in which an additional influence of the C-enriched austenite and the C-depleted martensite is expected.

The objective of this study is to evaluate the effect of chemical composition and microstructure on the corrosion resistance of Q&P-produced martensitic stainless steels and, particularly, the combined effect of C-enriched austenite, C-depleted martensite and inclusions on the corrosion mechanisms. With that aim, Q&P microstructures of three different alloys differing in C, Mn, and microalloying (Ti and Nb) content were characterised. Local surface potential differences were investigated by atomic force microscopy (AFM) and scanning Kelvin probe microscopy (SKPFM). The composition of the formed passive film on the sample surface was analysed using X-ray photoelectron spectroscopy (XPS). The electrochemical behaviour of the Q&P steels was investigated with open circuit potential (OCP) and potentiodynamic polarisation (PDP) at an aerated 3.5 wt.% NaCl solution. Moreover, the evolution of localised corrosion initiation was conducted by in-situ scanning electrochemical microscopy (SECM) experiments by operating in substrate generation/tip collection (SG/TC) mode.

2. Experimental procedure

2.1. Materials

The Q&P steels investigated in this work were prepared in RINA-CSM (Italy), with a length of 250 mm (rolling direction), a width of 200 mm, and a thickness of 1.5 mm. The chemical composition of the three stainless steel samples is given in Table 1. Alloys 2C and 3C have the same alloy content but different carbon content. Alloy 3CMn is similar to alloy 3C but with increased Mn and microalloying additions. Specimens 20 mm in length and 15 mm in width were prepared by electrical discharge machining from the sheets with the long axis parallel to the rolling direction. The Q&P treatment (Fig. 1), optimised in our prior research [43], consisted of austenitising at 1100 °C for 15 min, followed by quenching to 160 °C for alloy 2C, 99 °C for alloy 3C and room temperature 25 °C for alloy 3CMn. The materials are then subjected to partitioning at 450 °C for 5 min, followed by a final quenching to room temperature.

2.2. Microstructural and compositional analysis

The surface of the samples was prepared by standard metallographic procedures and finished by OPS (Oxide Polishing Suspensions) polishing for 15 min. Optical microscopy (Digital Keyence VHX-5000 and optical LEICA DMLM) was used to characterise the surface and identify the regions of interest for further study. A FEGSEM CarlZeiss Crossbeam 550 scanning electron microscope (SEM) equipped with energy-dispersive X-ray spectroscopy (EDS) detector was used to characterise the microstructures and analyse the elemental composition of the samples (matrix and inclusions/particles). All SEM/EDS data were collected at a working distance of 8.5 mm and an accelerating voltage of 10 kV.

The fraction of austenite in the final microstructure was quantified by a LakeShore 7307 Vibration Sample Magnetometer (VSM) calibrated with a standard nickel specimen. Specimens for magnetisation measurements were machined with a cubic shape from the Q&P specimens with a weight of approximately 60 to 100 mg. Magnetisation curves at room temperature were measured by a stepwise change in the applied magnetic field from +1.6T to −1.6 T. The volume fraction of retained austenite was calculated with the formula below,

$$f_{RA} = 1 - M_{sat}^{QP} \Big/ \left(M_{sat}^{Fe} * X_{Fe}^{alloy} \right) \tag{1a}$$

where M_{sat}^{QP} is the saturation magnetisation of the investigated Q&P specimen, X_{Fe}^{alloy} is the iron content in the steel (in wt.%), and M_{sat}^{Fe} is the saturation magnetisation of pure Fe with BCC structure, which yields

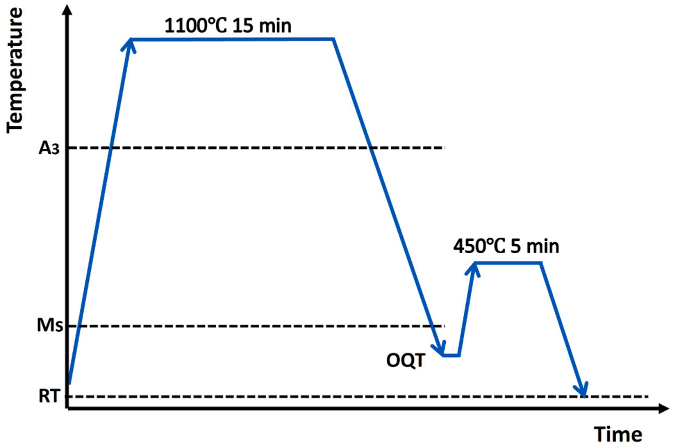

Fig. 1. A schematic presentation of the Q&P heat treatment, where A_3 indicates the temperature above which only austenite is present in the microstructure. M_S is martensite start temperature. QT is quenching temperature. RT is room temperature.

Table 1
Chemical composition of the steels, in wt.%.

Alloy	C	Mn	Si	Cr	Ni	Al	N	Nb	Ti	Fe
2C	0.2	0.7	0.35	12.5	0.2	0.01	0.03	–	–	Bal.
3C	0.3	0.7	0.35	13.0	0.2	0.01	0.03	–	–	Bal.
3CMn	0.3	3.0	0.35	13.0	0.2	0.01	0.03	0.05	0.05	Bal.

215 Am^2/kg at room temperature [44,45].

X-ray photoelectron spectroscopy (XPS) measurements were conducted to analyse the chemical composition and relative fractions of the formed (hydro)oxide layers. Before XPS measurements, the passive layer was formed by potentiostatic polarisation at 0.1 V (vs. Eoc) for two hours in 3.5 wt.% NaCl solution. Subsequently, the pre-passivated samples were rinsed with ethanol and dried with compressed air. The XPS analysis was conducted using a PHI-Versaprobe III spectrometer equipped with an Al-source (1486.71 eV photon energy) and automatic neutraliser. The irradiation power of the X-ray beam was set to 23.8 W, and a take-off angle of 46° was applied. All the specimens were measured at two different locations on the surface (100 μm in diameter) to verify the homogeneity of the layer composition. The elemental composition was determined by XPS survey (high-sensitivity) spectra, combined with high-energy resolution spectra of O 1 s, C 1 s, N 1 s, Fe 2p, and Cr 2p atomic concentrations. The Shirley method was used for background subtraction, and peak deconvolution was performed using the PHI Multipack software (V9.0). Binding energies were corrected for possible charging effects by referencing the C 1 s (284.8 eV) peak.

2.3. Electrochemical analysis

Conventional electrochemical experiments using potentiodynamic polarisation (PDP) were performed. Before the measurements, samples were embedded in an epoxy resin. Part of the sample surface was masked off by lacquer or covered by tape to control the exposing area and prevent possible crevice corrosion during the measurements. The exposed area was measured using images taken with a digital optical microscope (Keyence VHX-5000). All electrochemical experiments were performed using a Biologic VSP-300 potentiostat supported by EC-Lab V11.36 software. The experimental setup was a three-electrode cell, using an Ag/AgCl/KCl(sat.) electrode as a reference electrode (RE), a platinum mesh as a counter electrode (CE), and the sample as the working electrode (WE). Prior to PDP measurement, the open circuit potential (OCP) was measured for 1.5 h, at which steady-state is achieved. The potential scan rate was 0.167 mV/s from −200 mV vs. OCP until the breakdown potential. Aerated 3.5 wt% NaCl aqueous solution was used as the electrolyte, and measurements were carried out at room temperature (∼20 °C). At least four repetitions were carried out to confirm the reproducibility of the experiments.

2.4. Ex-situ and in-situ probe microscopy experiments

The SKPFM measurements were performed in the tapping mode using a Bruker Dimension Edge™ instrument with Nanodrive v8.05 software. A rectangular conductive cantilever (silicon pyramid single-crystal tip coated with PtIr5, SCM-Pit probe) was employed. Utilizing the tapping mode, the surface topography signal was recorded in the first (or forward) scan. Then, the tip was lifted to 100 nm and the Volta potential signal was recorded in the second (or backward) scan by following the topography contour in the first scan. All AFM/SKPFM measurements were performed at a scanning area of 50 × 50 $μm^2$ with a scan rate of 0.3 Hz and a pixel resolution of 512 × 512. The raw data was analysed using Gwyddion 2.60 software.

The SECM measurements were carried out using the Scanning Electrochemical Workstation SCV370 model (Princeton Applied Research, AMETEK Inc.). The tip for measurements was glass-insulated, disk-shaped platinum microelectrode which was fabricated from 10 μm diameter Pt wires (Sensolytics Inc.). An Ag/AgCl/KCl (sat.) was used as the reference electrode (RE), and a platinum wire as the counter electrode (CE). All the potentials in the experiments were referred to the reference electrode. The SECM operating in Sample Generation/Tip Collection (SG/TC) mode was used. The experiments were carried out in a solution containing 10 mM KI as a mediator and 0.1 M NaCl. The probe was polarised at 0.6 V to initiate the reaction of the mediator (I^-/I_3^-). Maps were obtained at a scan rate of 10 μm/s and a tip-sample distance of approximately 5 μm. In the SECM measurement, the I^-/I_3^-redox mediator was used to detect the electroactivity over S-rich inclusions. The chemical/electrochemical reactions are summarised in the following equations [28–31].

MnS Dissolution / Reduction

$$MnS + 2Cl^- \rightarrow MnCl_2 + S^{2-} \quad (1)$$

$$S^{2-} + H^+ = HS^- \quad (2)$$

$$2MnS + 4Cl^- + 3H_2O \rightarrow S_2O_3^{2-} + 2MnCl_2 + 6H^+ + 8e^- \quad (3)$$

SECM Tip oxidation

$$3I^- \rightarrow I_3^- + 2e^- \quad (4)$$

$$I_3^- + HS^- \rightarrow 3I^- + H^+ + S \quad (5a)$$

$$I_3^- + 2S_2O_3^{2-} \rightarrow 3I^- + S_4O_6^{2-} \quad (5b)$$

At the inclusion, MnS undergoes chemical or electrochemical dissolution to produce either hydrosulfide, as presented in reactions (1) and (2), or thiosulfate in reaction (3). To detect HS^- or $S_2O_3^{2-}$, I_3^- generated at the SECM tip is reduced to I^- by either HS^- or $S_2O_3^-$. Thus, the current at the SECM microelectrode is amplified in the presence of the dissolved sulfur species due to an increase of I^- at the microelectrode tip.

3. Results

3.1. Microstructure characterisation

Fig. 2 shows the SEM microstructure after OPS polishing of the three alloys after Q&P treatment, respectively. VSM measurements show that there is 11 % retained austenite in alloy 2C, and 22 % retained austenite in alloys 3C and 3CMn. Retained austenite cannot be distinguished in these SEM images. In alloys 2C and 3C, small black particles identified as MnS inclusions with sizes less than 1 μm embedded in the matrix are observed, as indicated in Fig. 2**a** and **b** with red arrows. In alloy 3CMn, the microstructure contains MnS inclusions, NbC inclusions (white particles with sizes less than 1 μm in Fig. 2**c**), and TiN inclusions (large rectangle and/or triangle with size up to 10 μm in Fig. 2**d**). Ten random OM micrographs (173 μm × 130 μm) were taken from each sample to quantify the prior austenite grain size (PAGS) and the density of the above-mentioned small MnS inclusion. The PAGS of alloy 3CMn (21.7 ± 4.1 μm) is smaller than that of alloys 2C and 3C (37.7 ± 9.7 μm and 36.2 ± 16.7 μm, respectively), due to the grain refinement role of the precipitates formed from micro-alloying elements [17].

A semi-quantitative analysis of the density distribution of small MnS (< 1 μm) particles shows that the number of particles per mm^2 is 23 ± 6 in alloy 2C, 16 ± 10 in alloy 3C, and 2 ± 1 in alloy 3CMn. The NbC particles are out of the OM view, therefore the NbC was not quantified. Therefore, the inclusion (small MnS and NbC) density of alloy 3CMn should be higher than the statistical results above. In addition, elongated MnS inclusions with a length of 10 μm to 100 μm were also observed in all three alloys and were unevenly distributed, so they were not quantified either.

EDS analysis was performed on those particles, and representative EDS spectra are presented in the supplementary information (**Figure S1**). The average chemical composition of similar particles in each sample is summarised in Table 2. For all three alloys, the ratio of Mn to S in the MnS inclusions if of approximately 1:1. The big particles with a characteristic square or triangle shape were identified as TiNb(N) particles. With negligible Nb content, the TiNb(N) particle represents TiN inclusion (**Figure S1(c)**).

3.2. Chemical composition of oxide film by XPS analysis

XPS analysis was conducted to obtain the chemical composition of

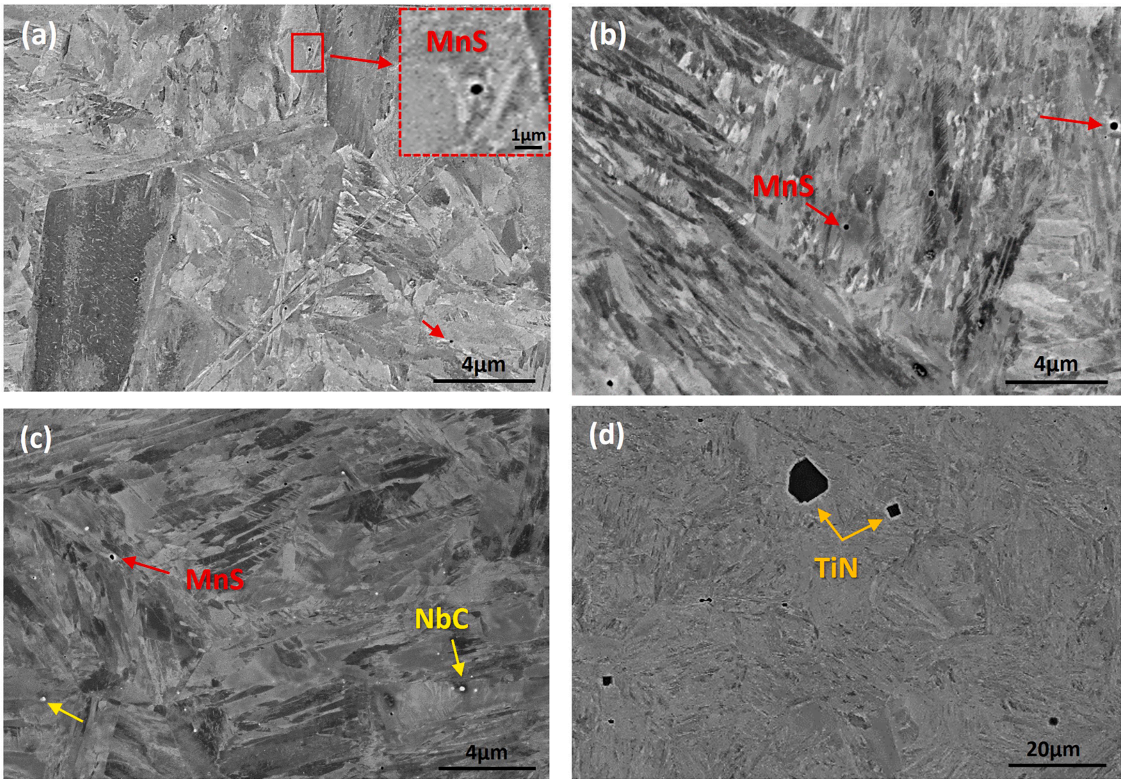

Fig. 2. SEM images of three studied alloys (a) alloy 2C, (b) alloy 3C, (c) & (d) alloy 3CMn.

Table 2
Chemical composition of inclusions obtained from EDS in three alloys (at.%).

Sample		Mn	S	Ti	Nb	N
Alloy 2C	MnS	16.3 ± 5.9	15.5 ± 4.9	–	–	–
Alloy 3C	MnS	2.5 ± 1.4	2.3 ± 2.1	–	–	–
Alloy 3CMn	MnS	36.7 ± 2.5	28.4 ± 1.7	–	–	–
	TiN	–	–	51.4 ± 0.4	0.8 ± 0	46.3 ± 1.6

the formed oxide layer on the pre-passivated samples. The XPS high-resolution survey scan showed that the passive film consists of the main elements Fe and Cr (Fig. 3). The XPS high-resolution scans show intense signals of Fe2p3 and Cr2p3 peaks, which are the main elements constituting the passive film [46,47]. The XPS spectra of individual elements were deconvoluted into an optimum number of peaks based on their binding energies. The deconvoluted fitting results of Fe2p3 and Cr2p3 spectrums in all three alloys are displayed in Fig. 3. For all three samples, the Fe2p3 spectra are composed of oxide peaks (FeO at ~709 eV and Fe_2O_3 at ~711 eV) and a metal peak (Fe(0) at ~707 eV), coupled with a Fe-hydroxide peak FeOOH at ~ 713 eV [46,49,50]. Additionally, an extra satellite peak at ~ 715 eV is also present, which has been previously reported in the literature [51,52]. The Cr2p3 spectra are composed of broad oxide peaks (Cr_2O_3 at ~576 eV, and CrO_2 at ~575 eV) and metal peak (Cr at ~573 eV), coupled with a small hydroxide peak ($Cr(OH)_3$ at ~577 eV).

The quantitative XPS analysis combines the Fe/Cr ratio with a fraction of deconvoluted components (Fig. 4). Generally, the passive layer showed a high fraction of Fe_2O_3 without significant differences between alloys for all three alloys. Alloys 2C and 3C have an almost identical passive layer. Alloy 3CMn contains 10 % less Fe_2O_3 and 6 % more Cr oxide. This might be caused by the grain size refinement (high tangled dislocation density) in alloy 3CMn, which provides fast diffusion channels for Cr, thereby a relatively homogeneous distribution of Cr, and consequently, more Cr oxide can be formed. Although the particle density of MnS inclusions in alloy 3CMn is lower than that of alloys 2C and 3C, there is no certain correlation between the component and particle density in the passive film of these three alloys.

3.3. *Electrochemical characterisation*

To assess the electrochemical behaviour of the samples, OCP and potentiodynamic polarisation experiments were performed in an aerated 3.5 wt% NaCl solution. The representative results are presented in Fig. 5**a** and **b**, respectively. The OCP values were measured for 1.5 h to ensure a stable value. From the curves in Fig. 5**a**, all samples have a potential that steadily increases with time, suggesting the formation of the passive film on the sample surface. The results shown in Fig. 5**a** are a representative curve among the five repetitions for each sample.

Potentiodynamic polarisation gives insight into the kinetics of the corrosion process and the pitting resistance of the samples. From the curves in Fig. 5**b**, all samples exhibit the immediate formation of the passive region followed by a breakdown at higher potential. The current density increases drastically, indicating that the passive film has failed and pitting is detected on the sample surface. For alloys 2C and 3C, the passive region shows a stable current density. Alloy 3CMn shows transients in the current density, indicating the presence of metastable pitting during polarisation. Furthermore, alloy 3CMn exhibits an earlier breakdown of the passive region compared to alloys 2C and 3C.

For a quantitative comparison of the corrosion performance of the three alloys, the corrosion current density (i_{corr}), pitting potential (E_{pit}), and potential range of the passive region (E_{pit}-E_{corr}) were extracted and plotted in Fig. 5**c** and **d**. The corrosion current density values, shown in Fig. 5**c**, did not exhibit a significant difference between the samples considering the average value and scatter. No relation can be concluded between the different compositions or microstructure (phase fraction or inclusions). Overall, the three alloys showed very low current density (order 10^{-8} Acm^2) which is expected for these types of stainless steels

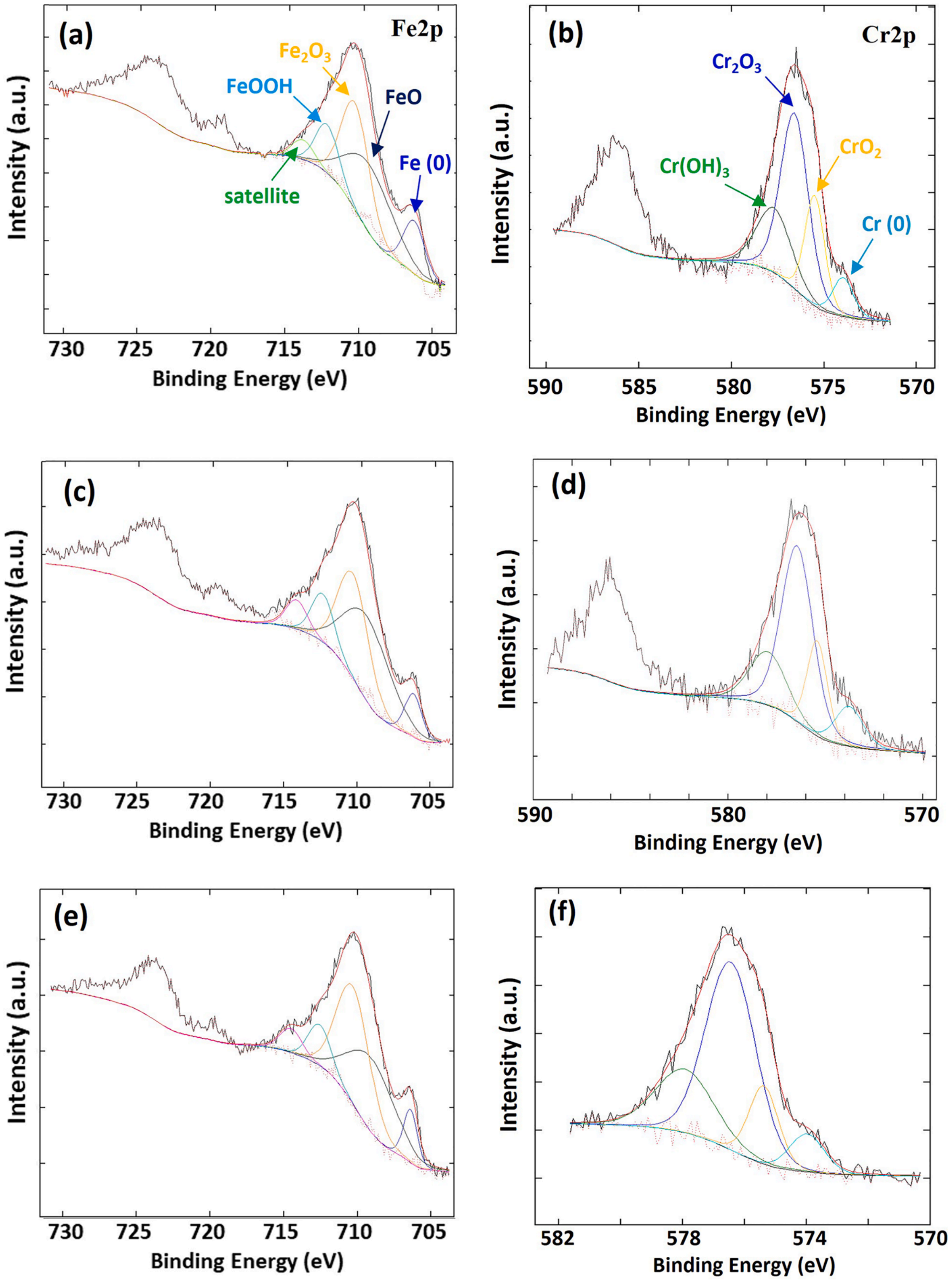

Fig. 3. Deconvolution results of Fe2p and Cr2p spectra in alloy 2C(a)(b), alloy 3C(c)(d), and alloy 3CMn(e)(f), respectively.

[14]. Fig. 5**d** shows the passive region and the pitting potential for each alloy. Alloys 2C and 3C show wider range of passivity compared to alloy 3CMn.

3.4. Surface potential characterisation by SKPFM

The topography and surface potential maps of the matrix for the three alloys were obtained by AFM/SKPFM measurements. The resulting maps are shown in Fig. 6. The dashed line in the maps highlights some selected martensite laths, which are visible in the topography maps (Fig. 6**a, d**, and **g**). Samples were polished with OPS, which led the hard martensite phase (laths) to stand out from the surface, showing a higher height and brighter colour on the topography map than the austenite. In contrast, the retained austenite phase is relatively softer, showing dark colour on the topography map. The Volta potential maps are displayed in Fig. 6**b**, **e**, and **h**. Selected line scans corresponding to both

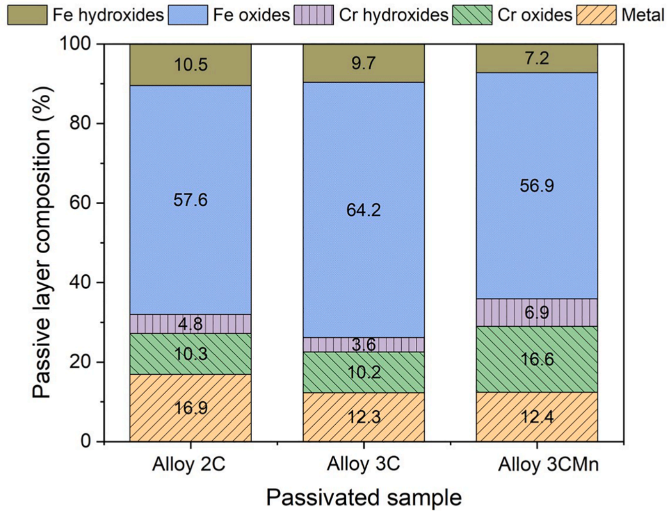

Fig. 4. Quantitative analysis of the composition of the oxide layer formed on the three alloys (2C, 3C, 3CMn) from the XPS fitting analysis.

topography and Volta potential are displayed in Fig. 6**c, f**, and **i**. Volta potential maps are plotted using a same potential scale for better comparison between the samples and to enhance the differentiation between martensite and austenite.

The potential maps reveal that martensite laths of all three alloys show lower potential compared to the austenite (darker). The line scan obtained from the marked martensite laths clearly shows topography peaks coinciding with potential drops. Among the entire scanning region, alloy 2C has Volta potential ranges from 8 to 20 mV; in alloy 3C, the potential range is similar to alloy 2C, ranging from 8 to 16 mV. In alloy 3CMn, the Volta potential ranges from 10 to 25 mV. The maximum potential difference between phases of the matrix is 15 mV. Generally, regions exhibiting lower surface potential values (directly linked to work function energy) are more prone to preferential dissolution or corrosion susceptibility than the matrix [53]. Therefore, the martensite in these three alloys may have all the preferential dissolution points when exposed to the corrosive environment.

Instead of the ideal Q&P microstructures containing retained austenite and martensite only, inclusions were also observed in the investigated heat-treated microstructures, especially MnS and TiN inclusions. SKPFM maps of the MnS inclusions in the three specimens are shown in Fig. 7. Fig. 7**a, e,** and **i** display the SEM image of elongated MnS inclusion on the sample surface of each alloy, while the topography maps in Fig. 7**b, f,** and **j** show corresponding size and morphology. Fig. 7**c, g,** and **k** display the Volta potentials maps of the three alloys. MnS inclusions show a lower Volta potential than the matrix. Line scans over the MnS inclusions are shown in Fig. 7**d, h,** and **l**, displaying potential differences of up to 35 mV were measured across MnS in alloy 2C, 40 mV in alloy 3C, and 30 mV in alloy 3CMn. The potential difference measured over the MnS inclusion is greater than the difference observed between phases (maximum 15 mV in Fig. 6). This indicates that the effect of inclusion is more dominant than phase fraction. Moreover, the Volta potential maps show local differences in the particles.

Fig. 8 presents the SEM/EDS and SKPFM maps of micro-alloying TiN inclusion on the surface of alloy 3CMn. Contrary to the MnS inclusions, TiN inclusion has a much greater Volta potential value than the matrix, a

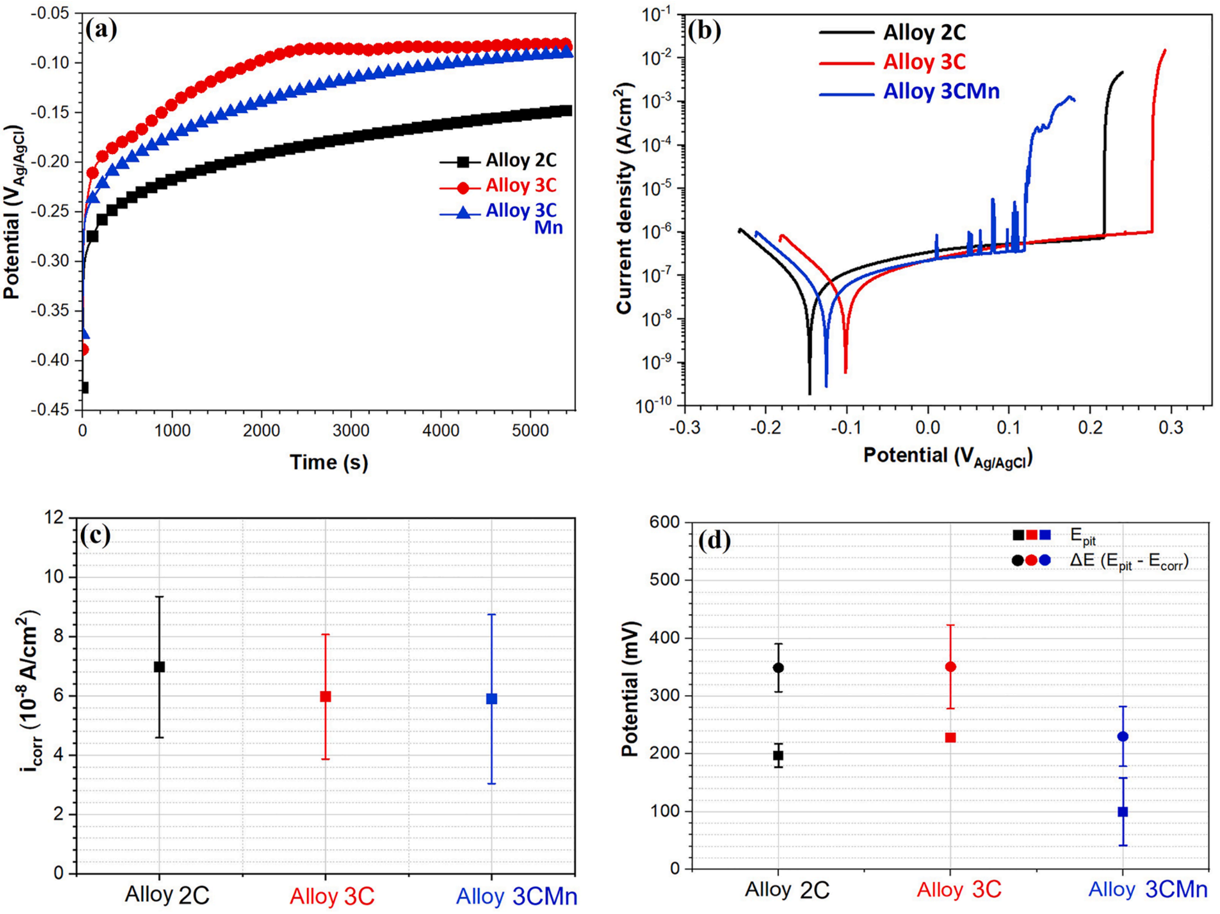

Fig. 5. Representative (a) OCP and (b) potentiodynamic polarisation curves of the three different alloys. The average values of (c) corrosion current density obtained by Tafel extrapolation and (d) pitting potential (E_{pit}) and passive region (ΔE). Experiments were repeated at least four times to confirm reproducibility.

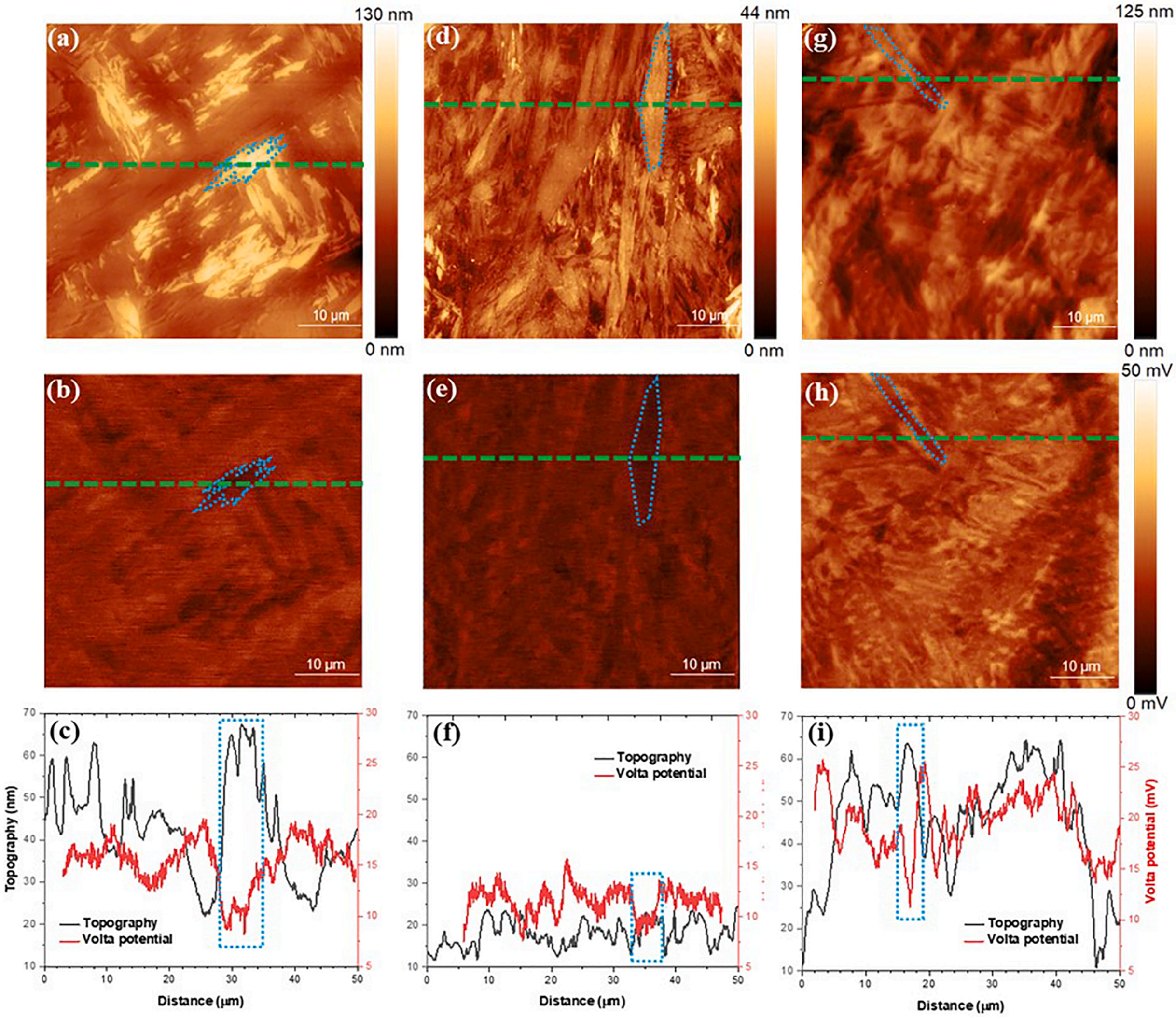

Fig. 6. Topography map, Volta-potential map, and extracted line profiles of the matrix without inclusions for (a)–(c) alloy 2C, (d)–(f) alloy 3C, and (g)–(i) alloy 3CMn, respectively.

difference of above 40 mV. This surface potential value implies a lower electrochemical activity of TiN than the matrix during exposure to electrolytes. Previous studies on interstitial-free steels, which have a ferritic matrix with a body-centered cubic (BCC) crystal structure and an low carbon content, have reported that TiN inclusions exhibit cathodic behavior [41,42,54], and the potential difference is the driving force for galvanic corrosion to occur at the surrounding matrix.

Round particle inclusions of MnS and NbC with dimensions less than 1 μm, such as the ones shown in Fig. 2, were not detected by topography or Volta potential maps. Due to the existence of large (> 10 μm) MnS and TiN inclusions, the round particle inclusions in such a small size do not cause a detectable effect.

3.5. In situ electrochemical measurements by SECM

Both SKPFM and PDP analyses proved that MnS and TiN inclusions may decline the corrosion performance of these alloys due to localised corrosion attacks. However, there is still a lack of direct evidence. Therefore, SECM measurements were performed to monitor the local electrochemical activity of inclusions. A large MnS inclusion was marked by indents (hardness tester indentation pit as positioning point) in alloy 2C, and a MnS inclusion with a nearby TiN inclusion was marked in alloy 3CMn. Fig. 9 shows SECM mappings operating in SG/TC mode on the surface of alloys 2C and 3CMn during immersion in 0.1 M NaCl.

The SECM maps clearly showed the variation of the current peak with the increase of the immersion times. For alloy 2C (region 1), Fig. 9**a**, the immersion time was of only 5 min. The current pointed by the black arrow corresponding to the MnS inclusion of ~4 nA indicates that the dissolution of the MnS inclusion starts immediately. After 1.5 h, the peak current is ~8 nA. After 3 h of immersion, the peak current was measured of ~15.5 nA, indicating the fastest dissolution rate of the MnS inclusion. The higher current indicates deletion of S^{-} in solution. After immersion for 5 h, the peak current starts decreasing to ~7 nA, when the dissolution process was slow down. The indents marked area includes a long MnS inclusion of about 100 μm (region 2) and three TiN particles (region 3). For alloy 3CMn, Fig. 9**b**, in 5 min, the SECM peak current of the big MnS inclusion reached ~4 nA. After immersion for 1 hour, the peak current increased to ~6 nA, and after immersion for 2 h, the peak current increased to ~21 nA. Then, it dropped to ~5 nA after immersion for 4 h and remained constant until the end of the measurement (6 h). After 6 h, Fig. 9**b** showed a strong signal around hardness indents. The dissolution rate in alloy 3CMn (two hours from 4 to 21 nA) is faster than in alloy 2C (three hours from 4 to 16 nA). This explains the earlier pitting initiation, i.e., the lower pitting potential in alloy 3CMn that was observed in PDP curves.

Fig. 9**c** and **d** present the OM images of both alloys after the SECM measurements. In both samples, the MnS inclusion is still present. Post-SECM EDS analysis confirmed the presence of S at the MnS sites, as

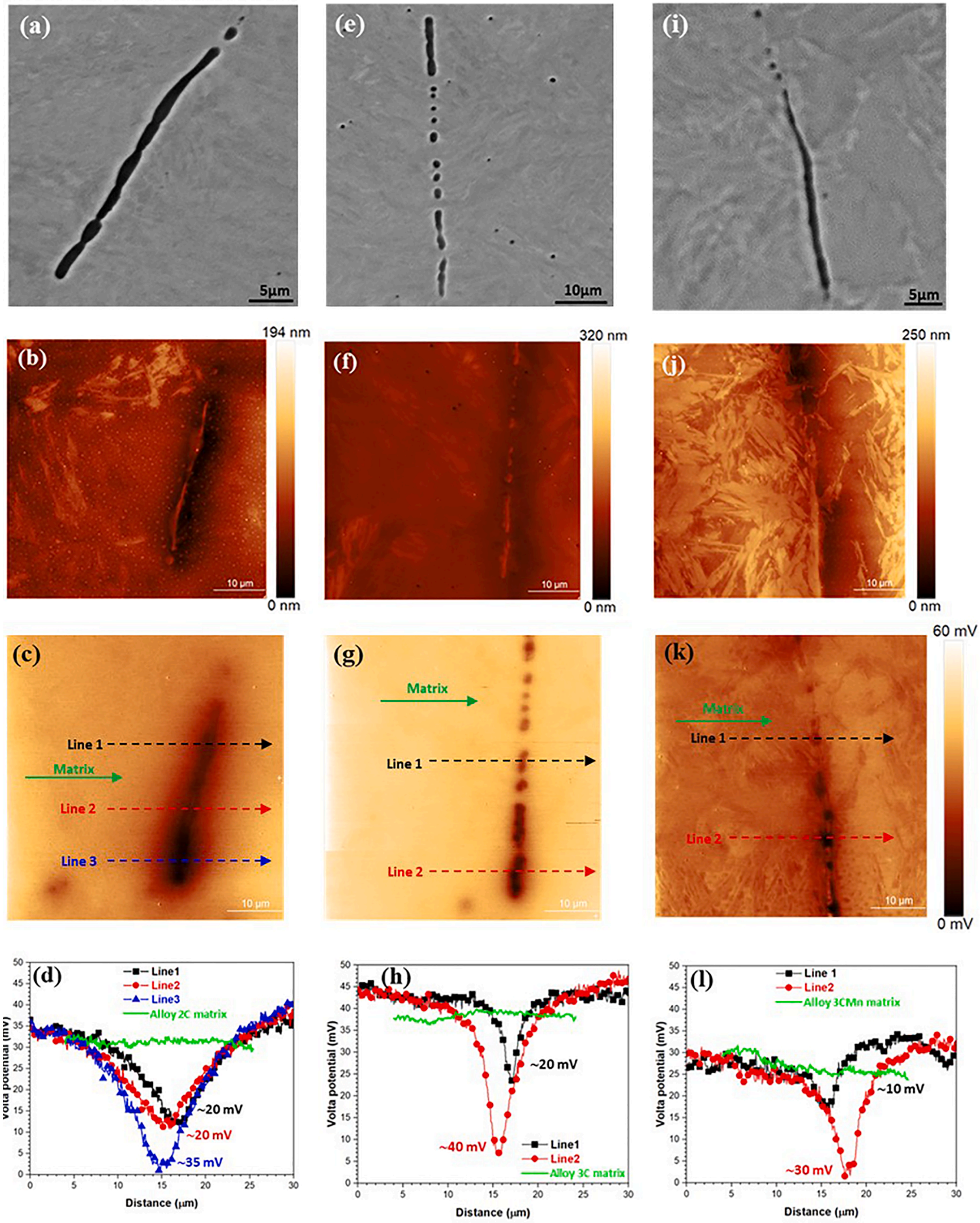

Fig. 7. SEM images, Topography and Volta-potential maps, and corresponding surface potential line profiles of elongated MnS inclusions in (a-d) alloy 2C, (e–h) alloy 3C, and (i–l) alloy 3CMn.

shown in the OM images of Fig. 9**c** and **d**. From region 3, the OM image clearly shows the remaining TiN inclusion, and one side of its surrounding matrix was corroded. This is in agreement with the surface potential results. NbC particles precipitate and epitaxially grow on the pre-existing TiN particles, forming a so-called "core-shell" configuration [18,33], becoming preferable sites for dissolution.

4. Discussion

The comparison between the corrosion performance of alloys 2C and 3C provides information regarding the effect of carbon content. The difference in chemical composition and quenching temperature leads to the difference in phase fractions with higher retained austenite in alloy 3C. Despite this, the SEM observation and XPS analysis indicated that

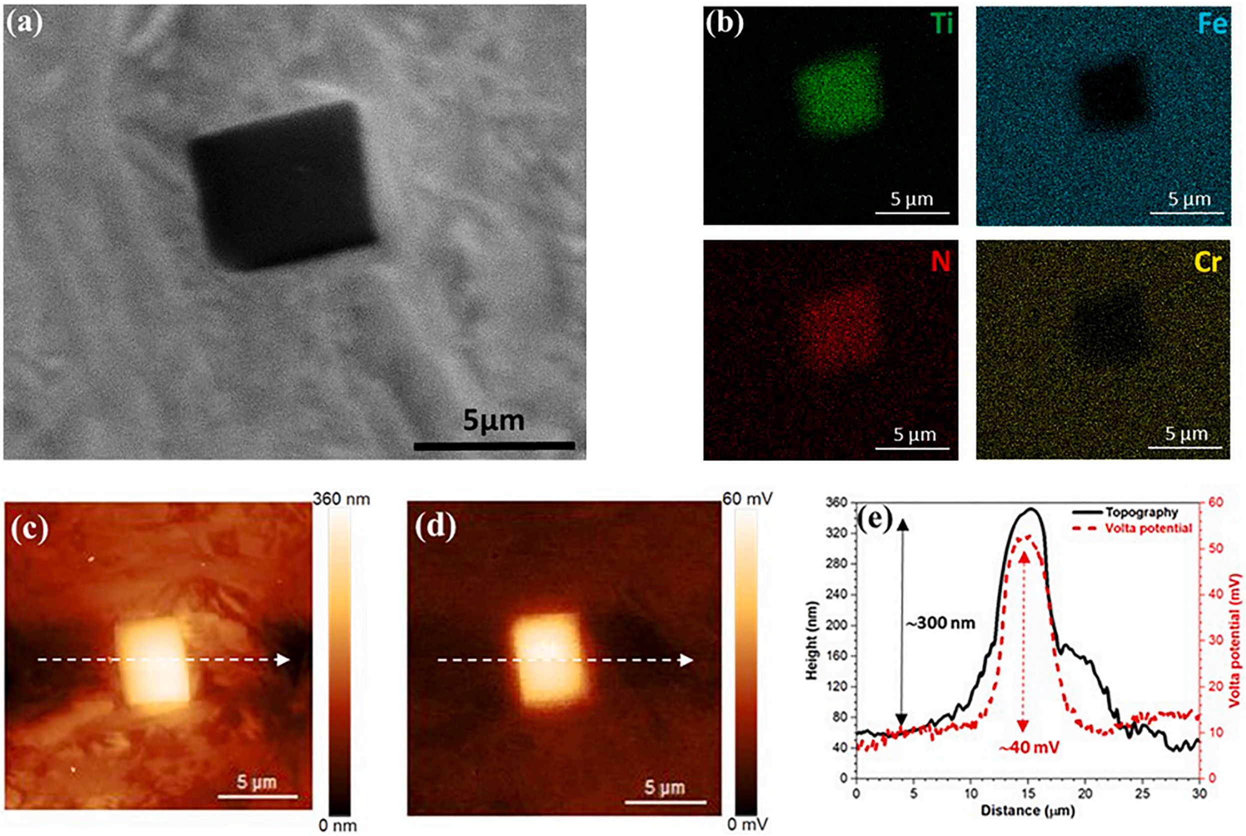

Fig. 8. (a) SEM, (b) EDS, (c) topography, (d) Volta potential maps, and (e) corresponding surface potential line profiles of NbTi-riched inclusion in alloy 3CMn.

these two alloys have similar microstructural characteristics (Fig. 2) and passive layer constituents (Figs. 3 and 4). As a result, the corrosion properties based on pitting potentials did not explicitly show a difference (Fig. 5). Alloys 3C and 3CMn have the same carbon content and equal phase fractions of retained austenite. However, alloy 3CMn exhibits the lowest E_{pit} value and the lowest passive region (Fig. 5**d**). Fig. 5**b** and **d** show that the addition of Mn, Nb and Ti makes the alloy more susceptible to pitting corrosion, which can be attributed to the existence of MnS and/or TiN inclusions, as observed in Fig. 2. As discussed in the literature [14,18,20], the presence of inclusions significantly influences the properties of the native or electrochemically formed passive layer. Not only will they influence the formation and stability of the oxide (e.g. composition, electrochemical properties, semi-conductor properties), but they also can play a crucial role in the initiation of localised corrosion such as pitting corrosion [55]. The Volta potential maps in Figs. 6–8 confirmed that the potential difference between inclusion and matrix is more pronounced than between martensite and retained austenite, which confirms that the inclusions play a dominant influencing role even in multiphase Q&P steels.

MnS round particles were observed in the three alloys with sizes less than 1 μm in diameter. Alloy 3CMn also contains NbC particles of the same size. They are fairly distributed in the microstructures, as shown in Fig. 2, and no difference in electrochemical behaviour among these micro-scale MnS particles was observed. Some of the MnS particles are present in elongated shapes with sizes of up to 100 μm. It was found that these long MnS inclusions can lead to the defection of the passive film, which has barely been reported [48].

The elongated MnS inclusions are present in all three alloys, but only alloy 3CMn showed transients of current density in potentiodynamic (Fig. 5**b**) polarisations, indicating the metastable pitting and the earlier breakdown which could be attributed to the additional pressence of TiN inclusions [56–58]. Figs. 7,8 show that the MnS inclusions have lower surface potential than the matrix, while the TiN site has much higher surface potential than the matrix. These differences in surface potential values might drive a selective dissolution of the matrix (in the case of TiN) or dissolution of MnS.

Fig. 10 illustrates schematically the pit initiation mechanism at inclusions in alloy 2C and 3C (Fig. 10**a**) and alloy 3CMn (Fig. 10**b**).

- **Pit initiation in presence of MnS inclusion (alloys 2C and 3C).** The initial microstructure (stage 1) displays the matrix with one MnS inclusion on the sample surface. The existence of inclusion makes the passive film discontinuous because of the different constituents (Fig. 4). Stage 2 involves the exposition to a corrosive environment, in which the passive film and the MnS inclusion start dissolving and release sulphur species, which was detected by the SECM (Fig. 9). This is driven by its 35 mV lower surface potential with respect to the matrix (Fig. 7). The dissolution process of MnS (stage 3) produces sulphur (S) that decomposes on the sample surface, which was detected after the SECM test. The decrease in current may be related to the S decomposition on the sample surface.
- **Pit initiation in the presence of both MnS and TiN inclusions (alloy 3CMn).** The initial microstructure (stage 1) illustrates more discontinuity and less heterogeneity of passive film. The MnS inclusion displays the same behaviour as alloys 2C and 3C. The well-known MnS inclusion triggered localised corrosion in austenitic stainless steels [21–31] still applies in Q&P-processed multiphase steels. Dissolution of MnS inclusion and trenching of the TiN/matrix interface occurs, as shown in stage 2; this is driven by the 40 mV surface potential difference. When the trench grows deeper (stage 3), a stable pit forms, which explains the lower pitting potential in alloy 3CMn. Dissolution of MnS, and the trenching around the TiN may lead to pitting or repassivation overall, all of this makes alloy 3CMn more susceptible to localised attack.

The effect of TiN inclusions on corrosion performance has been

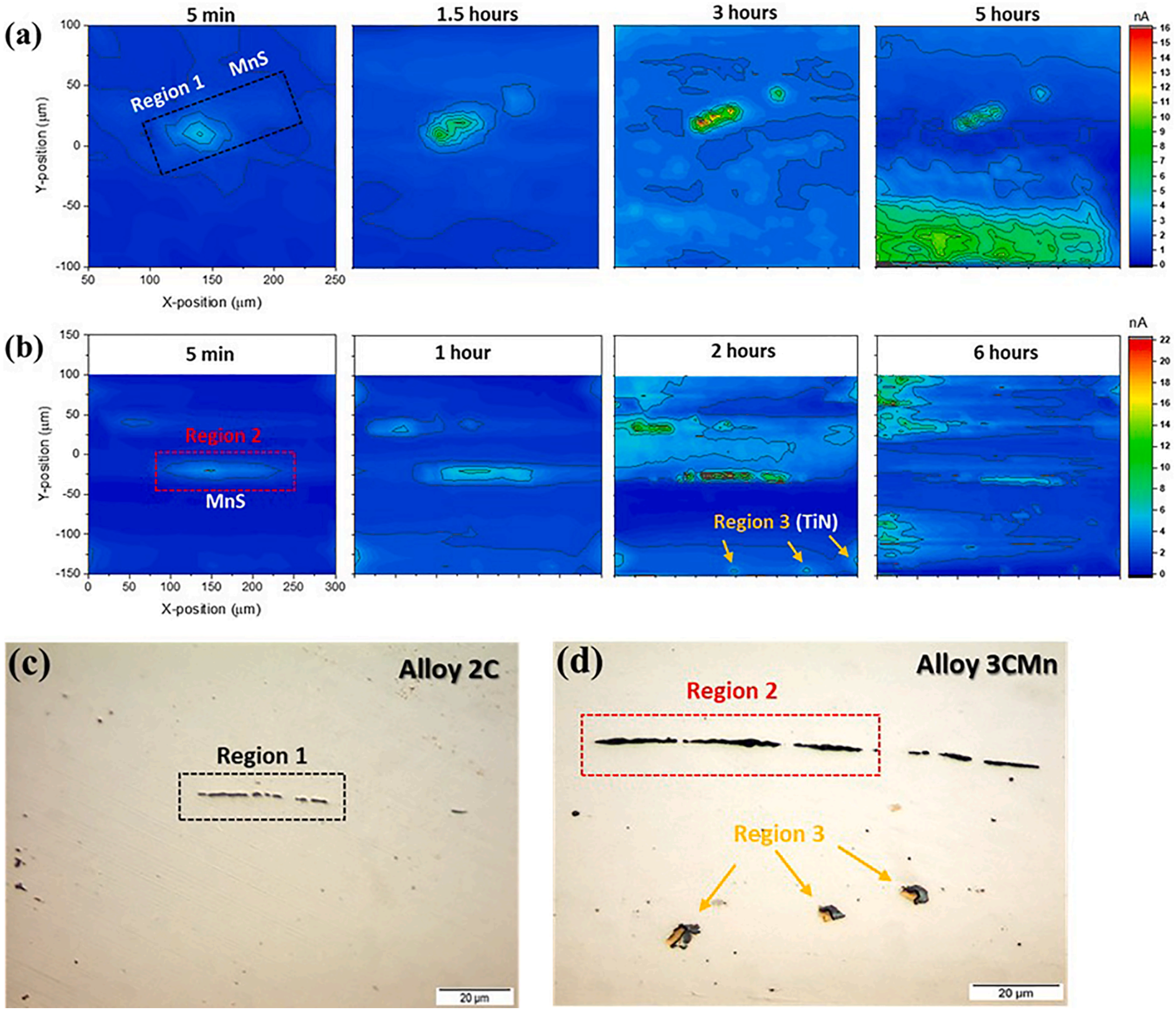

Fig. 9. Electrochemical current maps with an immersion time of alloys 2C (a) and 3CMn (b), and OM images after SECM measurements of alloy 2C(c) and alloy 3CMn(d), respectively. In alloys 2C and 3CMn, the scanning areas are 200 × 200 μm^2 and 300 × 250 μm^2, respectively.

widely investigated [41,42,57,58]. In austenitic stainless steels with an FCC structure and high C, Cr, and Ni content, TiN inclusions (often co-present with TiN—Ca complex inclusions) were found to have no effect on pitting performance [57,58]. However, in ferritic steels with a BCC structure, the TiN inclusion-induced pitting corrosion mechanism is well explained [41,42]. Step-like corrosion pits induced by TiN inclusions were observed using in situ techniques. These observations reveal that pitting corrosion initiates at the interface between the inclusion and the matrix [41,42], progressing through initiation, transition, and propagation stages, as summarized in previous studies [41]. The SECM measurement and microstructure observation in Fig. 9**b** and **d** confirmed that the TiN inclusion-induced corrosion mechanism can be extended to the multiphase Q&P-processed martensitic stainless steels.

In addition, microalloying elements refined the prior austenite grain size in alloy 3CMn, which further decreased its corrosion resistance because grain boundaries act as active sites promoting the metal dissolution and decreasing the stability of the passive layer on the sample surface [59,60].

5. Conclusions

The effect of chemical composition and microstructure on the corrosion resistance of Q&P-produced martensitic stainless steels was evaluated. Particularly, the combined effect of C-enriched austenite, C-depleted martensite and inclusions on the corrosion mechanisms was investigated by combining ex-situ and in-situ electrochemical techniques. The following conclusions are drawn.

- The corrosion resistance of Q&P steels is controlled mainly by the presence of inclusions, while chemical composition and phase fractions play a less prominent role. The strong influence of the inclusions is confirmed through SKPFM and potentiodynamic polarisation.
- The alloy displaying TiN and MnS inclusions displayed the worst corrosion resistance. The higher Mn content and grain refinement also contribute to this low corrosion performance.

CRediT authorship contribution statement

Gaojie Li: Writing – original draft, Investigation, Formal analysis, Data curation. **Ziyu Li:** Writing – review & editing. **Ehsan Rahimi:** Writing – review & editing. **Marta Muratori:** Writing – review & editing. **Ali Smith:** Writing – review & editing. **Maria J. Santofimia Navarro:** Writing – review & editing, Supervision, Project administration, Funding acquisition, Conceptualization. **Yaiza Gonzalez-Garcia:** Writing – review & editing, Supervision, Project administration, Funding acquisition, Conceptualization.

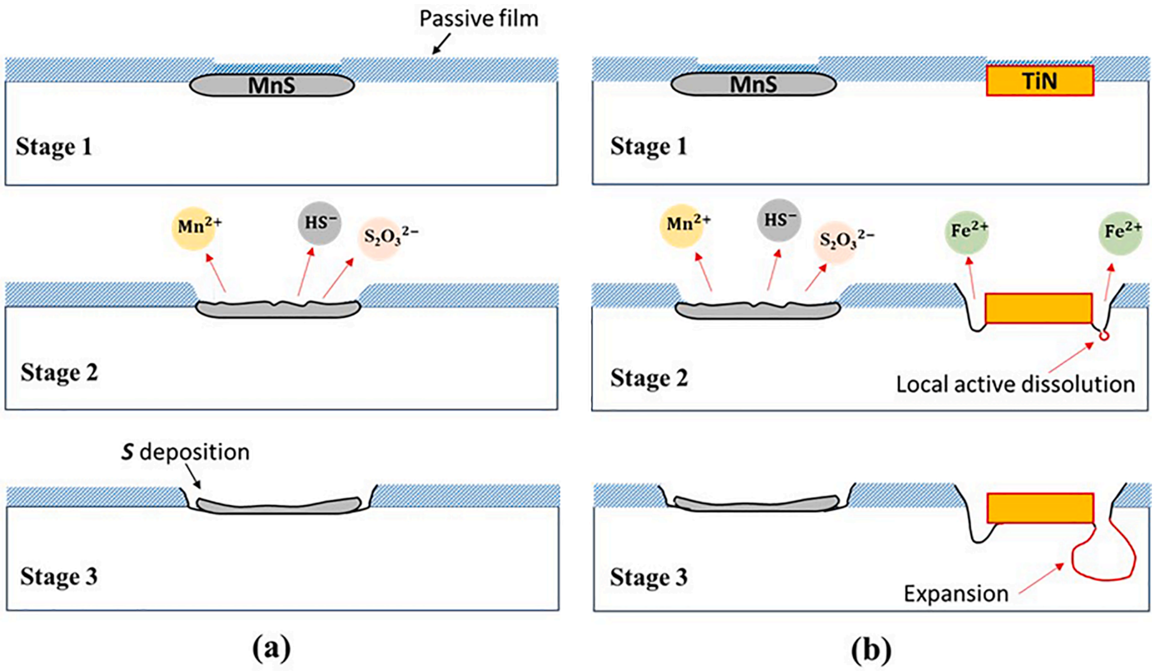

Fig. 10. Schematic illustration of the pit initiation mechanism at MnS and TiN inclusions in alloys 2C and 3C (a), and alloy 3CMn (b), respectively.

Declaration of competing interest

The authors declare that they have no known competing financial interests or personal relationships that could have appeared to influence the work reported in this paper.

Data availability

Data will be made available on request.

Acknowledgement

This research has received funding from the European Union Research Fund for Coal and Steel (RFCS) under grant agreement N 847195, QPINOX project. The authors gratefully acknowledge Kitty Baert and Tom Hauffman at the Vrije Universiteit Brussel for the XPS analysis, and Prasaanth Ravi Anusuyadevi (Delft University of Technology) for his contributions to both the XPS analysis and the subsequent discussions.

Supplementary materials

Supplementary material associated with this article can be found, in the online version, at doi:10.1016/j.electacta.2024.144646.

References

[1] D.K. Matlock, J.G. Speer, Third generation of AHSS: microstructure design concepts, microstructure and texture in steels (2009), pp.185–205, doi:10.1007/978-1-84882-454-6_11.
[2] X. Hu, Z. Feng, Report, 2021, https://doi.org/10.2172/1813170.
[3] S. Vögele, M. Grajewski, K. Govorukha, D. Rübbelke, Challenges for the European steel industry: analysis, possible consequences and impacts on sustainable development, Appl. Energy 264 (2020) 114633, https://doi.org/10.1016/j.apenergy.2020.114633.
[4] J.G. Speer, A.M. Streicher, D.K. Matlock, F. Rizzo, G. Krauss, Quenching and partitioning: a Fundamentally New Process to Create High Strength Trip Sheet Microstructures, The Iron & Steel Society, 2003, pp. 505–522.
[5] J.G. Speer, D.K. Matlock, B.C.D. Cooman, J.G. Schrothc, Carbon partitioning into austenite after martensite transformation, Acta Mater. 51 (2003) 2611–2622, https://doi.org/10.1016/S1359-6454(03)00059-4.
[6] J.G. Speer, F. Rizzo, D.K. Matlock, D.V. Edmonds, The "quenching and partitioning" process: background and recent progress, Mat. Res. 8 (2005) 417–423, https://doi.org/10.1590/S1516-14392005000400010.
[7] M. Hillert, J. Argen, On the definitions of paraequilibrium and orthoequilibrium, Scr. Mater. 50 (2004) 697–699, https://doi.org/10.1016/j.scriptamat.2003.11.020.
[8] J.G. Speer, D.K. Matlock, L. Wang, D.V. Edmonds, Quenched and partitioned steels, Compre. Mater. Proc. 1 (2014) 217–225, https://doi.org/10.1016/B978-0-08-096532-1.00116-3.
[9] J.G. Speer, E. De Moor, A.J. Clarke, Critical assessment 7: quenching and partitioning, Mater. Sci. Technol. 31 (2015) 3–9, https://doi.org/10.1179/1743284714Y.0000000628.
[10] L. Wang, J.G. Speer, Quenching and partitioning steel heat treatment, Metall. Microstr. Anal. 2 (2013) 268–281, https://doi.org/10.1007/s13632-013-0082-8.
[11] L. Yuan, D. Ponge, J. Wittig, P. Choi, J.A. Jiménez, D. Raabe, Nanoscale austenite reversion through partitioning, segregation and kinetic freezing: example of a ductile 2 GPa Fe–Cr–C steel, Acta Mater. 60 (2012) 2790–2804, https://doi.org/10.1016/j.actamat.2012.01.045.
[12] Q.L. Huang, C. Schröder, H. Biermann, O. Volkova, J. Mola, Influence of martensite fraction on tensile properties of quenched and partitioned (Q&P) martensitic stainless steels, Steel Res. Int. 87 (2016) 1082–1094, https://doi.org/10.1002/srin.201500472.
[13] T. Tsuchiyama, J. Tobata, T. Tao, N. Nakada, S. Takaki, Quenching and partitioning treatment of a low-carbon martensitic stainless steel, Mater. Sci. Eng. A. 532 (2012) 585–592, https://doi.org/10.1016/j.msea.2011.10.125.
[14] S.Y. Lu, K.F. Yao, Y.B. Chen, M.H. Wang, N. Chen, X.Y. Ge, Effect of quenching and partitioning on the microstructure evolution and electrochemical properties of a martensitic stainless steel, Corros. Sci. 103 (2016) 95–104, https://doi.org/10.1016/j.corsci.2015.11.010.
[15] J. Tobata, K.L. Ngo-Huynh, N. Nakada, T. Tsuchiyama, S. Takaki, Role of silicon in quenching and partitioning treatment of low-carbon martensitic stainless steel, ISIJ Int. 52 (2012) 1377–1382, https://doi.org/10.2355/isijinternational.52.1377.
[16] G. Luo, H.Y. Li, Y.G. Li, J.Q. Mo, Microstructures and properties of a low-carbon-chromium ferritic stainless steel treated by a quenching and partitioning process, Mater 12 (2019) 1704, https://doi.org/10.3390/ma12101704.
[17] A. Sierra-Soraluce, G. Li, M.J. Santofimia, J.M. Molina-Aldareguia, A. Smith, M. Muratori, I. Sabirov, Effect of microstructure on tensile properties of quenched and partitioned martensitic stainless steels, Mater. Sci. Eng. A. 864 (2023) 144540, https://doi.org/10.1016/j.msea.2022.144540.
[18] J.L. Yang, Y.F. Lu, Z.H. Guo, J.F. Gu, C.X. Gu, Corrosion behaviour of a quenched and partitioned medium carbon steel in 3.5wt.% NaCl solution, Corros. Sci. 130 (2018) 64–75, https://doi.org/10.1016/j.corsci.2017.10.027.
[19] T. Mehner, R. Morgenstern, P. Frint, I. Scharf, M.F.-X. Wagner, T. Lampke, Corrosion characteristics of a quenching and partitioning steel determined by electrochemical impedance spectroscopy, IOP Conf. Ser.: Mater. Sci. Eng. 373 (2018) 012003, https://doi.org/10.1088/1757-899X/373/1/012003.
[20] S.K. Bonagani, V. Bathula, V. Kain, Influence of tempering treatment on microstructure and pitting corrosion of 13 wt.% Cr martensitic stainless steel, Corros. Sci. 131 (2018) 340–354, https://doi.org/10.1016/j.corsci.2017.12.012.

[21] K. Eguchi, Quantitative analysis of initiation site of pitting corrosion on type 304 austenitic stainless steel, Corros. Sci. 221 (2023) 111312, https://doi.org/10.1016/j.corsci.2023.111312.

[22] Z. Duan, C. Man, H. Cui, Z. Cui, X. Wang, Formation mechanism of MnS inclusion during heat treatments and its influence on the pitting behavior of 316L stainless steel fabricated by laser powder bed fusion, Corros. Commun. 7 (2022) 12–22, https://doi.org/10.1016/j.corcom.2022.04.002.

[23] X. Huang, W. Qiu, B. Niu, X. Zou, L. Pan, C.T. Kwok, Role of complex nonmetallic inclusions on the localized corrosion resistance of wire arc additively manufactured super duplex stainless steel, J. Mater. Res. Technol. 28 (2024) 799–813, https://doi.org/10.1016/j.jmrt.2023.12.072.

[24] T. Suter, H. Böhni, A new microelectrochemical method to study pit initiation on stainless steels, Electrochim. Acta 42 (1997) 3275–3280, https://doi.org/10.1016/S0013-4686(70)01783-8.

[25] E.G. Webb, T. Suter, R.C. Alkire, Microelectrochemical measurements of the dissolution of single MnS inclusions, and the prediction of the critical conditions for pit initiation on stainless steel, J. Electrochem. Soc. 148 (2001) B186–B195, https://doi.org/10.1149/1.1360205.

[26] P. Schmuki, H. Hildebrand, A. Friedrich, S. Virtanen, The composition of the boundary region of MnS inclusions in stainless steel and its relevance in triggering pitting corrosion, Corros. Sci. 47 (2005) 1239–1250, https://doi.org/10.1016/j.corsci.2004.05.023.

[27] A. Chiba, I. Muto, Y. Sugawara, N. Hara, Pit initiation mechanism at MnS inclusions in stainless steel: synergistic effect of elemental sulfur and chloride ions, J. Electrochem. Soc. (2013) C511–C520, https://doi.org/10.1149/2.081310jes.

[28] C.H. Paik, H.S. White, R.C. Alkire, Scanning electrochemical microscopy detection of dissolved sulfur species from inclusions in stainless steel, J. Electrochem. Soc. 147 (2000) 4120–4124, https://doi.org/10.1149/1.1394028.

[29] T.E. Lister, P.J. Pinhero, The effect of localised electric fields on the detection of dissolved sulfur species from Type 304 stainless steel using scanning electrochemical microscopy, Electrochim. Acta 48 (2003) 2371–2378, https://doi.org/10.1016/S0013-4686(03)00228-7.

[30] Y.H. Yin, L. Niu, M. Lu, W.K. Guo, S.H. Chen, In situ characterisation of localised corrosion of stainless steel by scanning electrochemical microscope, Appl. Surf. Sci. 255 (2009) 9193–9199, https://doi.org/10.1016/j.apsusc.2009.07.003.

[31] M. Zhao, Z.H. Qian, Q.J. Qin, J.Y. Yu, Y.J. Wang, L. Niu, In situ SECM study on concentration profiles of electroactive species from corrosion of stainless steel, Corros. Eng. Sci. Technol. 48 (2013) 270–275, https://doi.org/10.1179/1743278212Y.0000000066.

[32] M. Charleux, W.J. Poole, M. Militzer, A. Deschamps, Precipitation behavior and its effect on strengthening of an HSLA-Nb/Ti steel, Metall Mater. Trans. A 32 (2001) 1635–1647, https://doi.org/10.1007/s11661-001-0142-6.

[33] I. Gutiérrez, effect of microstructure on the impact toughness of Nb-microalloyed steel: generalisation of existing relations from ferrite–pearlite to high strength microstructures, Mater. Sci. Eng. A 571 (2013) 57–67, https://doi.org/10.1016/j.msea.2013.02.006.

[34] X.J. Liu, J.C. Yang, C.K. Cai, A.X. Li, X. Lei, C.Q. Yang, Effect of microalloyed elements M (M = Ce, Ti, V, and Nb) on mechanical properties and electronic structures of γ-Fe: insights from a first-principles study, Steel Res. Int. 92 (2021) 2100053, https://doi.org/10.1002/srin.202100053.

[35] J. Webel, H. Mohrbacher, E. Detemple, D. Britz, F. Mücklich, Quantitative analysis of mixed niobium-titanium carbonitride solubility in HSLA steels based on atom probe tomography and electrical resistivity measurements, J. Mater. Res. Technol. 18 (2022) 2048–2063, https://doi.org/10.1016/j.jmrt.2022.03.098.

[36] Y. Zou, Y. Han, H.S. Liu, H.X. Teng, M.S. Qiu, F. Yang, Microstructure evolution and enhanced mechanical properties of a novel Nb-Ti micro-alloyed medium-Mn steel, Mater. Charact. 187 (2022) 111828, https://doi.org/10.1016/j.matchar.2022.111828.

[37] Y.J. Zhang, G. Miyamoto, T. Furuhara, Enhanced hardening by multiple microalloying in low carbon ferritic steels with interphase precipitation, Scr. Mater. 212 (2022) 114558, https://doi.org/10.1016/j.scriptamat.2022.114558.

[38] J.B. Tan, X.Q. Wu, E.H. Han, W. Ke, X.Q. Liu, F.J. Meng, X.L. Xu, Role of TiN inclusion on corrosion fatigue behavior of Alloy 690 steam generator tubes in borated and lithiated high temperature water, Corros. Sci. 88 (2014) 349–359, https://doi.org/10.1016/j.corsci.2014.07.059.

[39] D.H. Hur, J.H. Han, U.C. Lee, Y.S. Park, Microchemistry of Ti-carbonitrides and their role in the early stage of pit initiation of alloy 600, Corrosion 62 (2006) 591–597, https://doi.org/10.5006/1.3280673.

[40] M.B. Leban, R. Tisu, The effect of TiN inclusions and deformation-induced martensite on the corrosion properties of AISI 321 stainless steel, Eng. Fail. Anal. 33 (2013) 430–438, https://doi.org/10.1016/j.engfailanal.2013.06.021.

[41] H. Chen, L. Lu, Y.H. Huang, X.G. Li, Insight into TiN inclusion induced pit corrosion of interstitial free steel exposed to aerated NaCl solution, J. Mater. Res. Technol. 13 (2021) 13–24, https://doi.org/10.1016/j.jmrt.2021.04.046.

[42] P. Liu, Q.H. Zhang, Y. Watanabe, T. Shoji, F.H. Cao, A critical review of the recent advances in inclusion-triggered localised corrosion in steel, NPJ Mater. Degrad. 6 (2022) 81, https://doi.org/10.1038/s41529-022-00294-6.

[43] G. Li, C. Kwakernaak, A. Smith, M. Muratori, Y. Gonzalez-Garcia, M.J. Santofimia, Microstructure development of quenching and partitioning-processed martensitic stainless steels with different manganese content, Mat. Sci. Technol. 40 (2024) 449–465, https://doi.org/10.1177/02670836231215989.

[44] L. Zhao, N.H. van Dijk, E. Brück, J. Sietsma, S. van der Zwaag, Magnetic and X-ray diffraction measurements for the determination of retained austenite in trip steels, Mater. Sci. Eng. A 313 (2001) 145–152, https://doi.org/10.1016/S0921-5093(01)00965-0.

[45] A. Bojack, L. Zhao, P.F. Morris, J. Sietsma, In-situ determination of austenite and martensite formation in 13Cr6Ni2Mo super martensitic stainless steel, Mater. Charact. 71 (2012) 77–86, https://doi.org/10.1016/j.matchar.2012.06.004.

[46] M.C. Biesinger, B.P. Payne, A.P. Grosvenor, L.W.M. Lau, A.R. Gerson, R.St. C. Smart, Resolving surface chemical states in XPS analysis of first row transition metals, oxides and hydroxides: cr, Mn, Fe, Co and Ni, Appl. Surf. Sci. 257 (2011) 2717–2730, https://doi.org/10.1016/j.apsusc.2010.10.051.

[47] A. Barroux, T. Duguet, N. Ducommun, E. Nivet, J. Delgado, L. Laffont, C. Blanc, Combined XPS/TEM study of the chemical composition and structure of the passive film formed on additive manufactured 17-4PH stainless steel, Surf. Interfaces 22 (2021) 100874, https://doi.org/10.1016/j.surfin.2020.100874.

[48] A.R. Pratt, I.J. Muir, H.W. Nesbitt, X-ray photoelectron and Auger electron spectroscopic studies of pyrrhotite and mechanism of air oxidation, Geochim. Cosmochim. Acta 58 (1994) 827–841, https://doi.org/10.1016/0016-7037(94)90508-8.

[49] M. Vayer, I. Reynaud, R. Erre, XPS characterisations of passive films formed on martensitic stainless steel: qualitative and quantitative investigations, J. Mater. Sci. 35 (2000) 2581–2587, https://doi.org/10.1023/A:1004719213960.

[50] S. Marcelin, N. Pébère, S. Régnier, Electrochemical characterisation of a martensitic stainless steel in a neutral chloride solution, Electrochim. Acta 87 (2013) 32–40, https://doi.org/10.1016/j.electacta.2012.09.011.

[51] P.S. Bagus, C.J. Nelin, C.R. Brundle, B.V. Crist, N. Lahirie, K.M. Rosso, Origin of the complex main and satellite features in Fe 2p XPS of Fe_2O_3, Phys. Chem. Chem. Phys. 24 (2022) 4562–4575, https://doi.org/10.1039/D1CP04886D.

[52] D.N.G. Krishna, J. Philip, Review on surface-characterization applications of X-ray photoelectron spectroscopy (XPS): recent developments and challenges, Appl. Surf. Sci. Adv. 12 (2022) 100332, https://doi.org/10.1016/j.apsadv.2022.100332.

[53] E. Rahimi, A. Rafsanjani-Abbasi, A. Imani, A. Davoodi, TiO2/Cu2O coupled oxide films in Cl− ion containing solution: volta potential and electronic properties characterisation by scanning probe microscopy, Mater. Chem. Phys. 212 (2018) 403–407, https://doi.org/10.1016/j.matchemphys.2018.03.066.

[54] E. Rahimi, A. Rafsanjani-Abbasi, A. Imani, S. Hosseinpour, A. Davoodi, Correlation of surface Volta potential with galvanic corrosion initiation sites in solid-state welded Ti-Cu bimetal using AFM-SKPFM, Corros. Sci. 140 (2018) 30–39, https://doi.org/10.1016/j.corsci.2018.06.026.

[55] D. Kovalov, C.D. Taylor, H. Heinrich, R.G. Kelly, Operando electrochemical TEM, ex-situ SEM and atomistic modeling studies of MnS dissolution and its role in triggering pitting corrosion in 304L stainless steel, Corros. Sci. 199 (2022) 110184, https://doi.org/10.1016/j.corsci.2022.110184.

[56] S. Tokuda, I. Muto, Y. Sugawara, N. Hara, Effect of sensitization on pitting corrosion at MnS and CrS in Type 304 stainless Steel, J. Electrochem. Soc. 168 (2021) 091504, https://doi.org/10.1149/1945-7111/ac28c6.

[57] Y. Sun, X. Tan, R. Lan, G. Ran, J. Li, Y. Jiang, Mechanisms of inclusion-induced pitting of stainless steels: a review, J. Mater. Sci. Technol. 168 (2024) 143–156, https://doi.org/10.1016/j.jmst.2023.06.008.

[58] X. Tan, Y. Jiang, Y. Chen, A. Tong, J. Li, Y. Sun, Roles of different components of complex inclusion in pitting of 321 stainless steel: induction effect of CaS and inhibition effect of TiN, Corros. Sci. 209 (2022) 110692, https://doi.org/10.1016/j.corsci.2022.110692.

[59] G. Palumbo, D. Dunikowski, R. Wirecka, T. Mazur, U. Lelek-Borkowska, K. Wawer, J. Banaś, Effect of grain size on the corrosion behavior of Fe-3wt.%Si-1wt.%Al electrical steels in pure water saturated with CO2, Materials (Basel) 14 (2021) 5084, https://doi.org/10.3390/2Fma14175084.

[60] M. Soleimani, H. Mirzadeh, C. Dehghanian, Effect of grain size on the corrosion resistance of low carbon steel, Mater. Res. Express 7 (2020) 016522, https://doi.org/10.1088/2053-1591/ab62fa.